10-19-2021

Hippocampal and thalamic afferents form distinct synaptic microcircuits in the mouse infralimbic frontal cortex.

Kourtney Graham

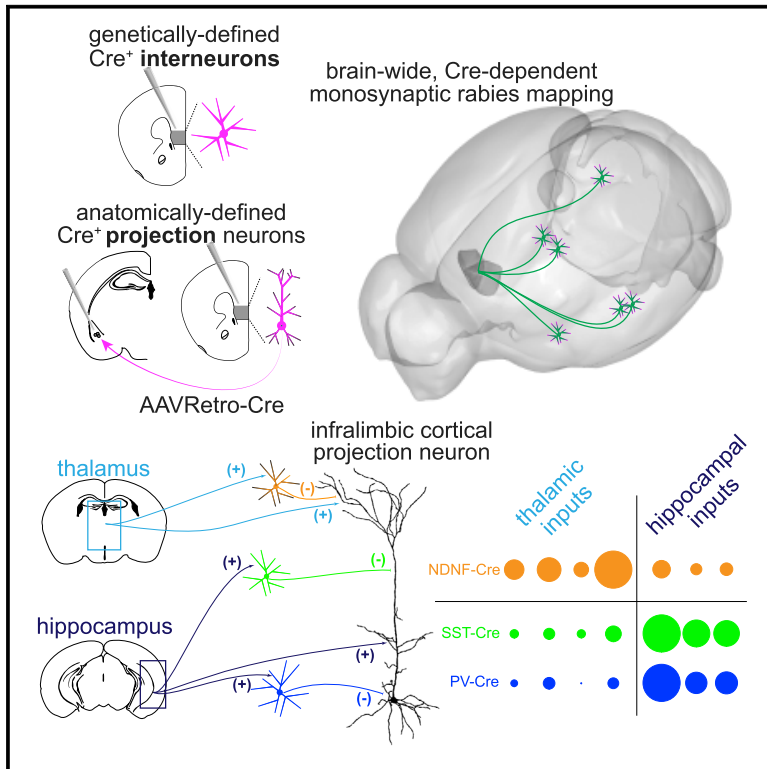Nelson Spruston

Erik B Bloss

Hippocampal and thalamic afferents form distinct synaptic microcircuits in the mouse infralimbic frontal cortex

Graphical abstract

Authors

Kourtney Graham, Nelson Spruston,
Erik B. Bloss

Correspondence

erik.bloss@jax.org

In brief

Patterns of synaptic connectivity govern the functional properties of neural circuits. Graham et al. map the afferent neurons targeting eight specific cell classes in mouse infralimbic cortex. Inputs from the hippocampus and thalamus are differentially targeted to specific neurons, suggesting two distinct synaptic microcircuits control circuit transformations.

Highlights

- Neurons in the infralimbic (IL) cortex mediate flexible forms of behavior

- IL neurons receive input from multiple brain regions

- Rabies mapping identifies inputs to inhibitory and excitatory neurons

- Hippocampal and thalamic afferents differentially target specific IL neurons

CelPress

Resource

Hippocampal and thalamic afferents form distinct synaptic microcircuits in the mouse infralimbic frontal cortex

Kourtney Graham,[2] Nelson Spruston,[1] and Erik B. Bloss[1,2,3,*]
[1]Howard Hughes Medical Institute, Janelia Research Campus, Ashburn, VA 20147, USA
[2]The Jackson Laboratory, 600 Main Street, Bar Harbor, ME 04609, USA
[3]Lead contact
*Correspondence: erik.bloss@jax.org
https://doi.org/10.1016/j.celrep.2021.109837

SUMMARY

The selection of goal-directed behaviors is supported by neural circuits located within the frontal cortex. Frontal cortical afferents arise from multiple brain areas, yet the cell-type-specific targeting of these inputs is unclear. Here, we use monosynaptic retrograde rabies mapping to examine the distribution of afferent neurons targeting distinct classes of local inhibitory interneurons and excitatory projection neurons in mouse infralimbic frontal cortex. Interneurons expressing parvalbumin, somatostatin, or vasoactive intestinal peptide receive a large proportion of inputs from the hippocampus, while interneurons expressing neuron-derived neurotrophic factor receive a large proportion of inputs from thalamic regions. A similar dichotomy is present among the four different excitatory projection neurons. These results show a prominent bias among long-range hippocampal and thalamic afferent systems in their targeting to specific sets of frontal cortical neurons. Moreover, they suggest the presence of two distinct local microcircuits that control how different inputs govern frontal cortical information processing.

INTRODUCTION

Neuronal circuits in the frontal cortex mediate some of the mammalian brain's most advanced forms of cognition, including the context-dependent selection of goal-directed behaviors (Miller, 2000). Logically, this function requires information relevant to the results from previous experiences (Hasegawa et al., 2000) as well as highly processed sensory information reflecting potentially new and relevant contextual cues. Electrical recordings from frontal cortex in awake, behaving animals have shown that individual frontal cortical neurons encode diverse representations of behaviorally relevant features, including sensory features, spatial locations, task temporal structure, and cues that predict previously rewarded or nonrewarded outcomes. Although the presence of these mixed representations in frontal cortex is intriguing (Hirokawa et al., 2019; Kennerley and Wallis, 2009; Machens et al., 2010; Rigotti et al., 2013), it remains unclear how such signals are generated.

These mixed representations could result from a neuroanatomical organization in which specific afferent information streams are connected to specific subsets of postsynaptic frontal cortical neurons. In this scenario, cell-type-specific forms of synaptic connectivity would provide a hardwired constraint on the possible representations generated by specific neurons, which is consistent with previous connectomics results demonstrating both cell-type and subcellular specificity and precision within circuit synaptic architectures (Bloss et al., 2018; Druck-

mann et al., 2014; Kasthuri et al., 2015). Conversely, all frontal cortical neurons might receive input from each afferent pathway yet produce mixed representations through cell-autonomous forms of synaptic plasticity or task-specific forms of neuromodulation. We sought to test which of these scenarios predominated on distinct sets of inhibitory and excitatory neurons in the mouse frontal cortex.

Generating brain-wide maps of connected neurons has been a major challenge for neuroscience given the submicrometer scale of synapses connecting two neurons but the 100- to 1,000-fold greater scale of axonal and dendritic processes within the brain (Lichtman and Denk, 2011). To circumvent the need for ultrastructural visualization of synaptic connections, the transsynaptic and retrograde transport properties of rabies viruses have been exploited to produce maps of connected neurons across long distances at cellular resolution (Luo et al., 2018; Ugolini, 2011; Wall et al., 2010; Wickersham et al., 2007). Moreover, the recent ability to deliver rabies-derived reagents to molecularly or anatomically defined cell types offer the potential to determine whether different cell types have distinct sets of inputs and outputs across the entire brain.

The extent to which rabies experiments can produce accurate maps of connected neurons is dependent on the efficiency of the transsynaptic retrograde transport. Nearly all cell-type-specific rabies mapping experiments have used a single genetically modified strain of rabies virus (SAD); recently, Reardon and colleagues (Reardon et al., 2016) have shown that the CVS strain of

rabies permits significantly greater labeling of long-range connected circuits. Here, we took advantage of this property of the CVS variant to perform cell-type-specific, monosynaptic, retrograde rabies tracing in an effort to determine the brain-wide input patterns to specific cell classes in the infralimbic (IL) region of the mouse frontal cortex. Using targeted knockin Cre driver lines, we mapped the brain-wide pattern of afferent neurons forming synapses on IL interneurons expressing parvalbumin (PV), somatostatin (SST), vasoactive intestinal peptide (VIP), and neuron-derived neurotrophic factor (NDNF). Using a AAVRetro-Cre strategy to gain genetic access to projection neurons (Tervo et al., 2016), we also mapped the brain-wide pattern of afferent neurons targeting specific IL excitatory projection neurons. Specifically, we chose IL projection neurons targeting the basolateral amygdala (BLA), lateral entorhinal cortex (LEC), nucleus reuniens of the thalamus (RE), or periaqueductal gray (PAG) because they have been implicated in a common IL-dependent function: the top-down control over the expression of fear-related behaviors (Bloodgood et al., 2018; Ramanathan et al., 2018; Rozeske et al., 2018; Xu et al., 2012).

Consistent with the notion that the CVS variant provides higher transsynaptic efficiency at synapses forming long-range pathways, our results strongly suggest that neurons in IL cortex receive inputs predominantly from long-range afferent circuits. This differs substantially from published findings using SAD rabies virus (Ährlund-Richter et al., 2019; Sun et al., 2019) that concluded connectivity to mouse frontal cortex is dominated by local cortical circuits. Our brain-wide connectivity maps support a model in which specific IL neurons receive afferent inputs from common upstream regions, yet the proportion of afferent neurons within each pathway varied across the cell classes. PV-Cre, SST-Cre, and VIP-Cre interneurons each receive the largest proportion of their afferent inputs from hippocampal area CA1, while the largest proportion of inputs to NDNF-Cre interneurons originate from RE. A similar dichotomy in the receipt of hippocampal and thalamic inputs remained evident across excitatory projection neurons. Because the interneurons examined here provide functionally distinct forms of inhibition targeted to different dendritic regions of IL projection neurons, our data suggest the presence of two spatially organized microcircuits that govern information transforms in IL projection neurons. Finally, we have created a public resource to accompany this publication, rabies-assisted interrogation of synaptic IL networks (or RAISIN; https://raisin.janelia.org), that provides analysis and visualization of these datasets. Ultimately, this resource should facilitate more targeted future experiments to relate the underlying structural features of frontal cortical cell types to their emergent functional computations.

RESULTS

Maps of IL inputs and outputs
To determine the diversity of cortical and subcortical inputs to and outputs from IL, we first made input and output maps from mouse IL cortex by direct injection of recombinant adeno-associated viruses (rAAVs) expressing fluorescent proteins that travel in a retrograde (i.e., RetroAAV; Tervo et al., 2016) or anterograde (i.e., rAAV2/1) manner and compared these results to those ob-

tained from fluorescent conjugated tracers (CTB-555 and WGA-555). Major inputs to the mouse IL cortex arise from area CA1 of the hippocampus, mediodorsal thalamus (Md-Th), RE, BLA, and neighboring regions within frontal cortex, all consistent with data from rat (Hoover and Vertes, 2007) and nonhuman primate (Barbas, 2000; Ongür and Price, 2000). Conversely, the major IL outputs are neighboring regions of the frontal cortex, the dorsomedial and ventral striatal regions, both Md-Th and RE, the lateral hypothalamus, and the BLA. IL circuits are thus organized as efferent-only pathways (e.g., IL-to-ventral striatum with no ventral striatum-to-IL connection), afferent-only pathways (e.g., CA1-to-IL projections with no IL-to-CA1 projection), or reciprocal loops (e.g., connections to and from Md-Th, RE, and BLA) (Figure S1).

Genetic and neuroanatomic access to nonoverlapping cell classes in IL cortex
These coarse input/output maps are useful insofar as they constrain the possible routes of information flow through mouse IL cortex. However, such maps lack the ability to discern whether afferent regions projecting to IL use similar or different patterns of connectivity onto specific postsynaptic cell types. Circuit mapping strategies that take advantage of the transsynaptic spread of rabies virus have been developed to answer precisely such questions. For these strategies to generate interpretable maps, however, they must be employed to distinct postsynaptic cell classes that have little to no minimal overlap. We used two different strategies to gain genetic access to distinct, nonoverlapping IL neurons. In the first, we used transgenic targeted knockin mice, where Cre recombinase was driven by the promoter of genes expressed in subsets of cortical interneurons. In the second, we used intracranial injections of RetroAAV-Cre in downstream IL target regions to drive Cre recombinase in IL projection neurons.

We first confirmed that PV-Cre (Hippenmeyer et al., 2004), VIP-Cre (Taniguchi et al., 2011), SST-Cre (Lovett-Barron et al., 2012), and NDNF-Cre (Tasic et al., 2016) driver lines permit genetic access to distinct sets of inhibitory interneurons in IL. Using triple-label *in situ* hybridization and confocal microscopy, we found that Cre expression within each driver line demonstrated high specificity and efficiency and that overlap between Cre-expressing neurons and marker genes for the other driver lines was low (<1% in all comparisons for all lines) (Figures 1A–1C). PV-Cre, VIP-Cre, SST-Cre, and NDNF-Cre neurons differed in terms of the laminar location within IL (Figure S2), and reconstruction of virus-labeled neurons from these Cre driver lines demonstrated large differences in their dendritic morphology (Figures 1C and S2).

In the absence of Cre driver lines for different projection neurons, we gained genetic access via axonal transduction of a new designer AAVRetro virus optimized for retrograde transport (Tervo et al., 2016) (in a manner similar in spirit to Schwarz et al., 2015). To determine the overlap between IL projection neurons, we visualized pairs of projection neurons using a viral dual-recombinase approach in which AAVRetro-Cre and AAVRetro-FlpO were injected into separate downstream targets and labeled in IL with Cre- and FlpO-dependent viral fluorescent reporters. We found that all four sets of projection neurons were
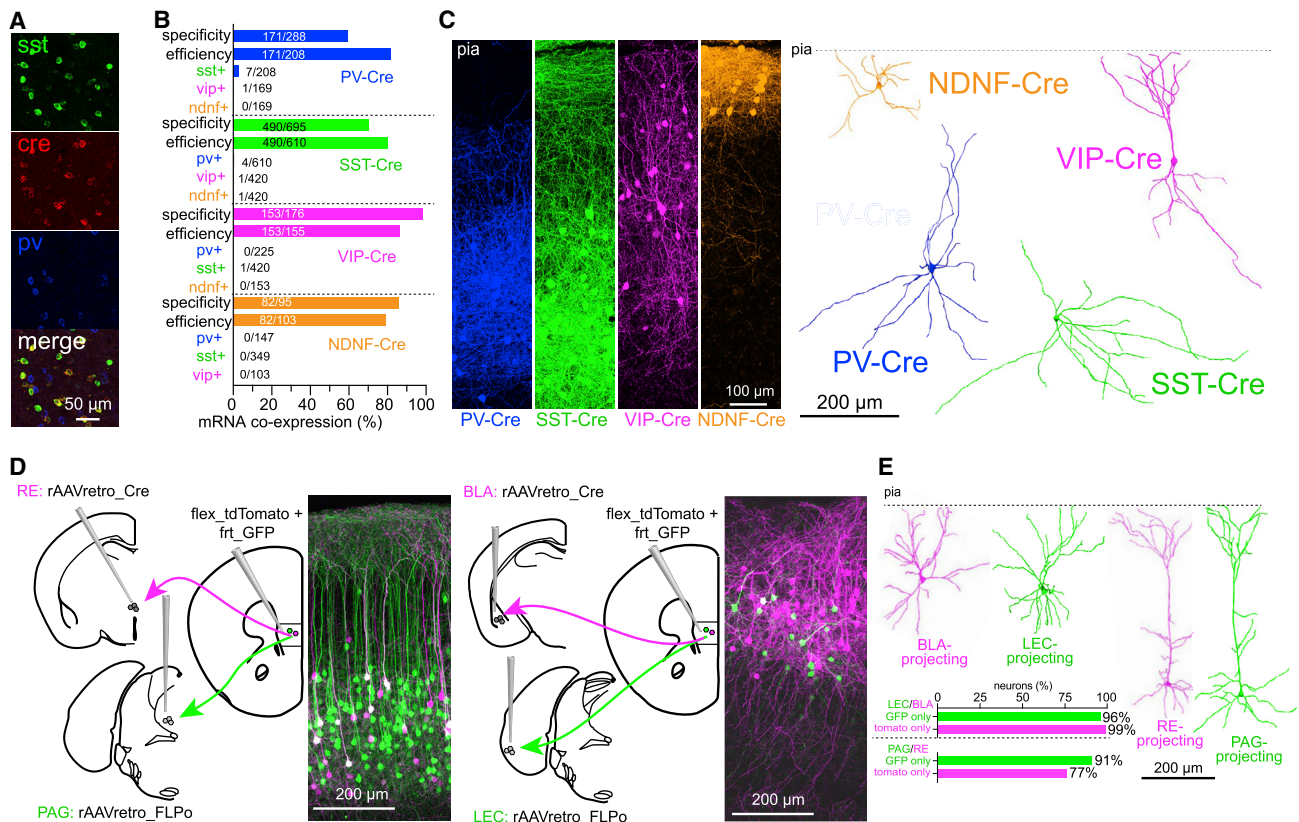
Figure 1. Genetic and neuroanatomic access to distinct neurons in IL cortex

(A) Example of a triple-label fluorescence *in situ* hybridization experiment from an SST-Cre mouse with fluorescent *in situ* probes labeling *sst*, *cre*, and *pv* transcripts. Scale bar, 50 μm.

(B) Quantification of the specificity, efficiency, and marker gene expression overlap across each Cre driver line in IL cortex (number and proportion of cells shown in each graph).

(C) Visualization of the neurons within these driver lines using a viral Cre-dependent GFP reporter (left; images are pseudocolored by line) permitted reconstruction of neuronal morphology (right); see Figure S2 and Data S1 for the quantification of soma locations and dendritic morphologies. Scale bar, 100 μm.

(D) Schematic showing labeling of IL projection neurons using a dual Cre and FLPo retrograde viral recombinase strategy. Scale bar, 200 μm.

(E) Reconstructions of the dendritic morphology of BLA-, LEC-, RE-, and PAG-projecting neurons and their cellular overlap; see Figure S2 and Data S1 for the quantification of soma locations and dendritic morphologies.

spatially intermingled in IL but arose from largely nonoverlapping populations of superficial (e.g., BLA-targeting and LEC-targeting) or deep-layer (PAG-targeting and RE-targeting) pyramidal cells (Figures 1D and 1E), consistent with previous reports from the adjacent dorsal PL region (Cheriyan et al., 2016; Collins et al., 2018; Little and Carter, 2013). Reconstructions of projection neurons demonstrated nearly identical dendritic morphologies within each superficial- or deep-layer pair (Figure S2), permitting a stringent comparison to be made across projection neurons with similar dendritic patterns. Thus, interneuron Cre driver lines and RetroAAV-Cre transduction of projection neurons permit genetic access to nonoverlapping cell classes within the mouse IL cortex.

Quantification of RabV starter cells

To transduce Cre-expressing neurons with CVS-N2cΔG GFP(EnvA) RabV (Reardon et al., 2016), two Cre-dependent AAVs were injected into IL, one encoding the TVA receptor required for entry of the modified RabV and the other encoding

the N2c glycoprotein required for RabV transsynaptic movement. Both of these AAVs also expressed the far-red fluorophore mKate2, permitting the identification of the neurons competent for subsequent RabV transduction and transsynaptic spread (i.e., "starter cells"). Neurons transduced by helper viruses and RabV express both GFP and mKate2, while RabV-labeled presynaptic neurons express GFP only (Figures 2A–2C). To quantify the number of mKate2$^+$ or GFP$^+$ cells, we developed a semiautomated analysis pipeline that aligns, thresholds, assigns, and counts fluorescently labeled neurons in individual brain regions according to Paxinos and Franklin (2004). Alignment and quantification in this manner produced nearly identical data when a subset of sections was aligned to the Allen Mouse Brain Atlas (Figure S3).

We validated this pipeline by experiments that revealed a low rate of false positive or false negatives compared to manual neuron counts (Figure S3). We quantified and assigned the number of mKate2$^+$/GFP$^+$ double-labeled starter cells near the injection sites and found these starter cells were enriched in IL cortex across all mice from both interneuron classes and projection
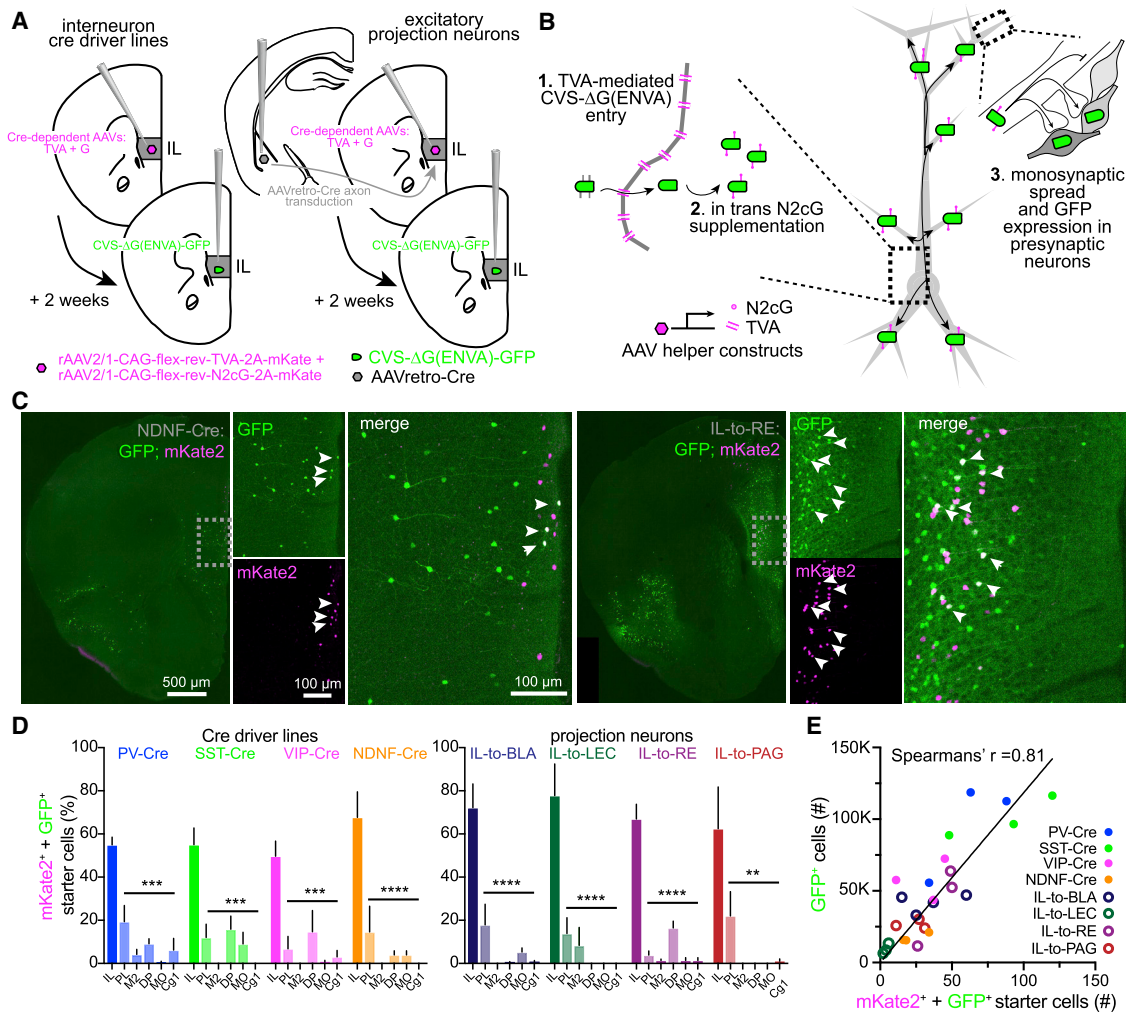
Figure 2. Labeling afferent neurons to specific neuronal subclasses

(A) The injection configuration differed across experiments that transduced RabV-competent starter cells in Cre driver lines (left) or projection classes (right). In experiments that sought to label projection neurons, an additional injection of AAVRetro-Cre into a downstream target was necessary to drive Cre expression in IL neurons.

(B) In both approaches, TVA and G are expressed via Cre-dependent rAAVs to render specific neurons competent to take up and transport the CVS-N2c-ΔG(ENVA)-GFP.

(C) "Starter cells" at the injection site were identified by the dual expression of both mKate2 and GFP; the left four images are from an experiment with IL NDNF-Cre neurons (note the localization of starter cells to layer I), and the right four are from an experiment with IL-to-RE neurons (note the localization of starter cells to layer V). Scale bars in the NDNF images represent 500 μm (left), 100 μm (center panels), and 100 μm (right) and also apply to the analogous images from the IL-to-RE sample.

(D) Starter cells were preferentially localized within IL relative to the neighboring cortical regions; data are presented as mean ± SEM. **p < 0.005; ***p < 0.001; ****p < 0.0001.

(E) Starter cell numbers correlated strongly with the total number of GFP-labeled presynaptic neurons.

(D) and (E) include data from n = 3 mice for each group, except for n = 4 mice in IL-to-BLA projections. See Figure S3 and Data S1 for additional information and statistical details.

neuron experiments (note that a small fraction of starter cells was found in the neighboring prelimbic cortex [located dorsal to IL] and dorsal peduncular cortex [located ventral to IL]) (Figure 2D).The total number of starter cells (summed across all regions) correlated strongly with the numbers of presynaptic neurons labeled by RabV-GFP (interneurons: n = 12, Spearman r = 0.83, p = 0.0015; virus-labeled projection neurons: n = 13, Spearman r = 0.79, p = 0.002; note 1 IL-to-BLA mouse was excluded from this

analysis due to poor mKate2 expression) (Figure 2E). The linear relationship between starter cell number and total GFP-labeled cell number was expected on account of the low numbers of starter cells in our experiments (mean, 38; range, 2–118).

To determine the viral "leak" in our CVS-N2cΔG GFP(EnvA) approach, we performed identical experiments in the absence of any transgenic or viral Cre expression (e.g., in WT mice with no AAVRetro-Cre). Since cortical neurons should not be competent
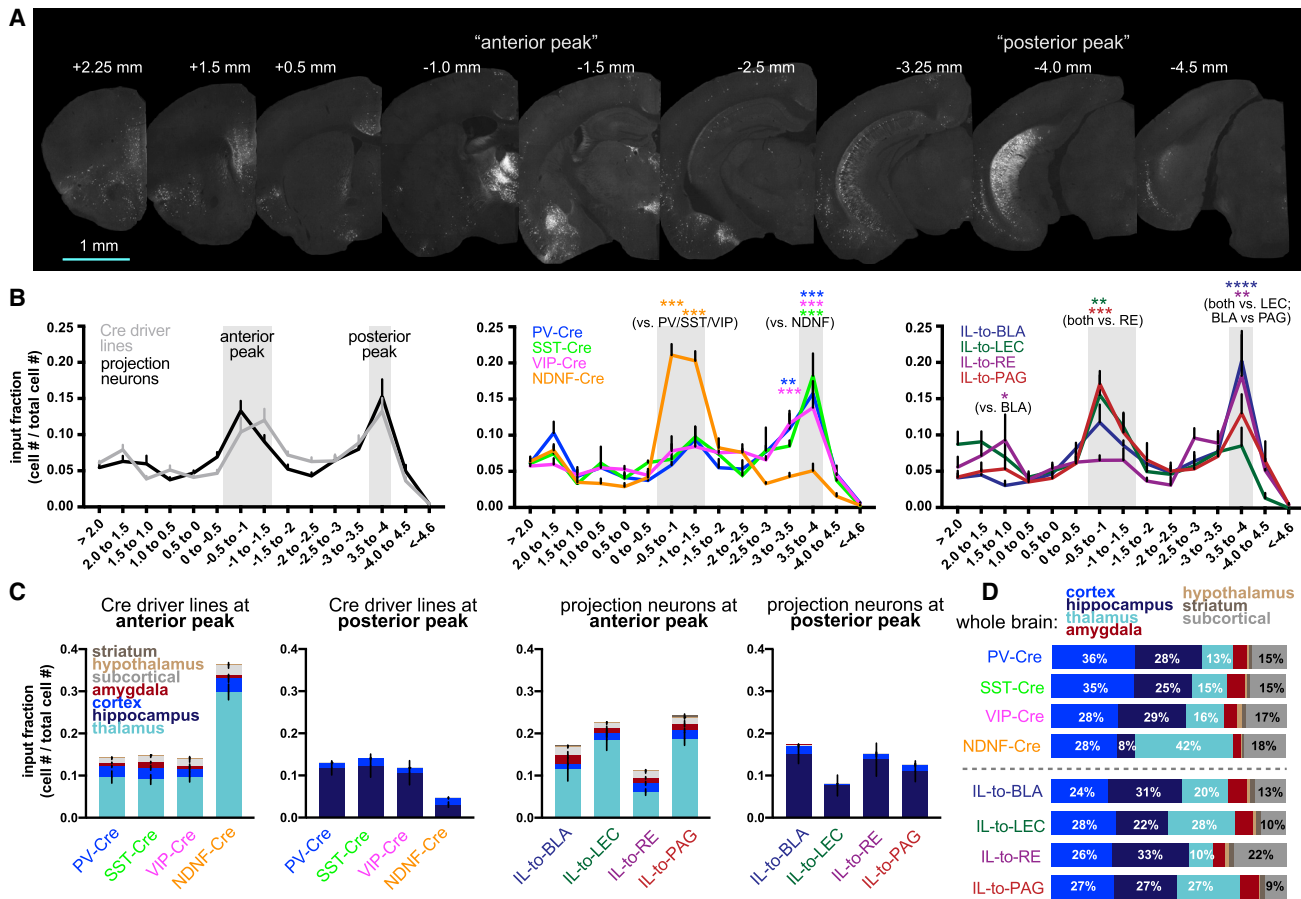
Figure 3. Spatial distribution of afferent neurons targeting different IL cell types

(A) Images from an IL-to-BLA sample showing presynaptic neurons along the anterior-posterior (A-P) axis with high density of neurons at −1.0 mm and −1.5 mm (referred to as the "anterior peak"), as well as at −4.0 mm (the "posterior peak"). Scale bar, 1 mm.

(B) Input fraction of GFP$^+$ neurons along the A-P axis between the pooled inhibitory Cre driver lines (n = 12 mice from the Cre lines and n = 14 from the excitatory projection classes) (left) among the inhibitory interneuron Cre driver lines (center) and among the excitatory projection neurons (n = 3 mice for each projection except for n = 5 mice in IL-to-BLA projections) (right). Plots are mean ± SEM. **p < 0.002; ***p < 0.0002; ****p < 0.0001.

(C) The proportion of input neurons that were assigned to the thalamus, hippocampus, cortex, amygdala, subcortical, hypothalamus, or striatum at the anterior and posterior peaks in the inhibitory Cre driver lines and in viral-labeled projection neurons. N's are the same as (B), and plots are mean ± SEM.

(D) A plot of the normalized percentage of afferent neurons from regions across the whole brain. N's are the same as (B). (B)–(D) include data from n = 3 mice for each group except for n = 5 mice in IL-to-BLA projections; plots are mean ± SEM.

See Figure S4 and Data S2 for additional information and statistical details.

to express the Cre-dependent helper constructs that were injected in IL, there should be very few GFP-expressing neurons. Consistent with this notion, these experiments yielded 488 ± 118 GFP$^+$ neurons (mean ± SEM, n = 3 mice) scattered across the mouse brain, suggesting a small but nonzero leak of our viral system (similar to Miyamichi et al., 2013; Weissbourd et al., 2014) (Figure S3). By contrast, the experiments with transgenic or viral Cre expression yielded 49,024 ± 6,698 GFP$^+$ labeled neurons (mean ± SEM, n = 26 mice) (Figure S3), suggesting that this leak contributes ∼1% of the total labeled neurons in an experimental sample.

Distribution of afferent neurons targeting IL inhibitory and excitatory neurons

We examined the spatial distribution of the GFP$^+$ input fraction (defined as cell number/total cell number) along the anterior-

posterior (A-P) axis of the brain from our inhibitory interneuron (n = 3 mice per genotype) and excitatory projection neuron (n = 3 mice per LEC, RE, and PAG projection classes; n = 5 mice per BLA projection class) datasets. When comparing the pooled inhibitory datasets to the pooled excitatory neuron datasets, the input fractions along the A-P axis were statistically indistinguishable (Figures 3A, 3B, and S4). Both datasets featured two prominent and well-separated peaks along the A-P axis, one that lies between 0.5 mm and 1.5 mm posterior to bregma (referred to herein as the "anterior peak") and a second that lies between 3.5 to 4.0 mm posterior to bregma (the "posterior peak"). These datasets suggest that the majority of presynaptic neurons targeting IL neuronal classes labeled by CVS-N2c-ΔG GFP(EnvA) RabV are long-range projection neurons (i.e., arise from outside local frontal cortical regions). This result differs dramatically from

previous IL or PL RabV experiments that concluded inputs to both inhibitory and excitatory neurons were predominantly made by local cortical neurons (Ährlund-Richter et al., 2019; Sun et al., 2019).

When we examined these distributions across the different inhibitory Cre driver lines, we found that PV-Cre, SST-Cre, and VIP-Cre neurons had virtually identical patterns of input fraction of presynaptic neurons along the A-P axis. The largest input fraction to these three interneurons was found at the posterior peak; in contrast, the largest proportion of input to NDNF-Cre neurons was found at the anterior peak (Figures 3B and S4). At both peaks, the magnitude of the effect was ~2-fold (i.e., the input fraction was ~2-fold larger for NDNF-Cre mice compared to PV-Cre/SST-Cre/VIP-Cre at the anterior peak and PV-Cre/SST-Cre/VIP-Cre neurons had a two-fold greater input fraction at the posterior peak; p < 0.0001 for each comparison) and was evident in each individual replicate (Figure S4). Among the excitatory projection classes, differences were also evident in the input fractions at the A-P axis peaks. Specifically, LEC- and PAG-projecting neurons had a larger input fraction at the anterior peak compared to RE-projecting neurons (p < 0.005 and p < 0.0005, respectively), while LEC-projecting neurons had a smaller input fraction at the posterior peak compared to BLA-projecting and RE-projecting neurons (p < 0.0001 and p < 0.005) (Figures 3B and S4).

We next examined how the input fractions within each peak related to brain structures (Figure 3C). At the anterior peak, all interneurons received the majority of inputs from the thalamus, yet NDNF-Cre neurons received an ~3-fold greater proportion of thalamic inputs compared to PV-Cre, SST-Cre, or VIP-Cre neurons. Conversely, at the posterior peak, all interneurons received the majority of inputs from the hippocampus, yet PV-Cre, SST-Cre, and VIP-Cre received ~3-fold greater inputs from hippocampal regions than NDNF-Cre neurons. Similar patterns were found among the projection neurons; LEC-projecting and PAG-projecting neurons received roughly 2-to-3-fold greater proportion of inputs from the thalamus than BLA- or RE-projecting neurons. Conversely, BLA- and RE-projecting neurons received ~2-fold greater inputs from hippocampal regions than LEC-projecting neurons. The differential receipt of inputs from neurons across brain structures at each peak was recapitulated when we considered the overall proportion of input neurons across the brain (Figure 3D). Collectively, these results show that IL neuron classes receive inputs from different proportions of neurons in the thalamus and hippocampus.

Regional differences in the proportion of afferent neurons targeting IL interneurons

We next considered the distribution of presynaptic neurons across functionally relevant groups of thalamic and cortical nuclei. We used a recently described taxonomy of thalamic regions (Phillips et al., 2019) to determine whether inputs from major thalamic nuclei differentially targeted IL interneurons. We found that regions in the secondary thalamic group (e.g., Md-Th, AM, VM, and VA) and RE (which forms its own distinct molecular class within the thalamus) each had a greater input fraction to NDNF-Cre neurons than neurons in the other three Cre driver lines (Figure 4A; Table 1). Using information modality to parse cortical regions into coarse functional groups (e.g., frontal asso-

ciation, motor, somatosensory, and visual), we found that both PV and SST-Cre mice had greater input fractions from frontal association regions compared to VIP or NDNF-Cre mice (Figure 4A).

We next examined the proportion of input neurons across all brain regions (n = 212). We found only a small number of regions that differed significantly different among PV-Cre, SST-Cre, and VIP-Cre neurons (PV versus SST, 7 regions; PV versus VIP, 5 regions; and SST versus VIP, 4 regions). However, PV-Cre, SST-Cre, and VIP-Cre driver lines each had a greater number of regions that differed in comparison to NDNF-Cre (PV-Cre versus NDNF, 15 regions; SST-Cre versus NDNF, 18 regions; and VIP-Cre versus NDNF, 12 regions) (Figure 4B). The largest individual input fraction to PV-Cre, SST-Cre, and VIP-Cre driver lines was from hippocampal area CA1 (~12%); however, the CA1 input fraction to NDNF-Cre neurons was only ~3% (p < 0.0001 for each line versus NDNF-Cre) (Figure 4B). In contrast, the largest input fraction to NDNF-Cre neurons was from RE (~13%), which was significantly greater than the RE input fraction to PV-Cre, SST-Cre, or VIP-Cre (~2%; p < 0.0001 for each versus NDNF). Moreover, we found a systematic underrepresentation of midline thalamic neurons (e.g., RE, AM, subthalamic, VM, and Md-Th) targeting PV-Cre, SST-Cre, and VIP-Cre driver lines relative to NDNF-Cre and a corresponding overrepresentation of hippocampal-associated regions (e.g., CA1, dorsal subiculum, and subicular transition region) targeting PV-Cre, SST-Cre, and VIP-Cre relative to NDNF-Cre (Figure 4C). Consistent with this notion, a principal-component analysis (PCA) revealed hippocampal and thalamic regions were among the top regions that contributed variability to the interneuron Cre driver line datasets (Figure S5).

We corroborated these differences among the Cre driver lines by using an orthogonal, correlation-based approach. In this approach, we restricted our analysis to regions in which at least one Cre driver line received >1% of the input fraction; this enabled us to avoid spuriously high correlations across the lines on account of the large numbers of afferent regions with near-zero values. We computed pairwise correlations (two-tailed Spearman's r) between Cre driver lines and compared these correlations to simulated values from shuffled datasets (Figure S5). The correlations among PV-Cre, SST-Cre, and VIP-Cre driver lines were high (r ~0.75 for each line) and within the shuffled distributions; however, the correlations between each of these driver lines compared to NDNF-Cre was substantially weaker than expected (i.e., outside the expected distribution of the shuffled datasets; PV versus NDNF: Spearman's r = 0.22; SST versus NDNF: Spearman's r = 0.19; VIP versus NDNF: Spearman's r = 0.35) (Figure S5). Collectively, these results reveal a dramatic shift between the primary afferent regions targeting IL cortical PV/SST/VIP interneurons from those targeting IL NDNF interneurons.

Differences among afferent regions targeting IL excitatory projection neurons

We performed similar analyses to determine the differential targeting of afferents to excitatory IL projection neurons. As in the interneuron datasets, we found that the largest proportion of input from the thalamus belonged to regions in the secondary
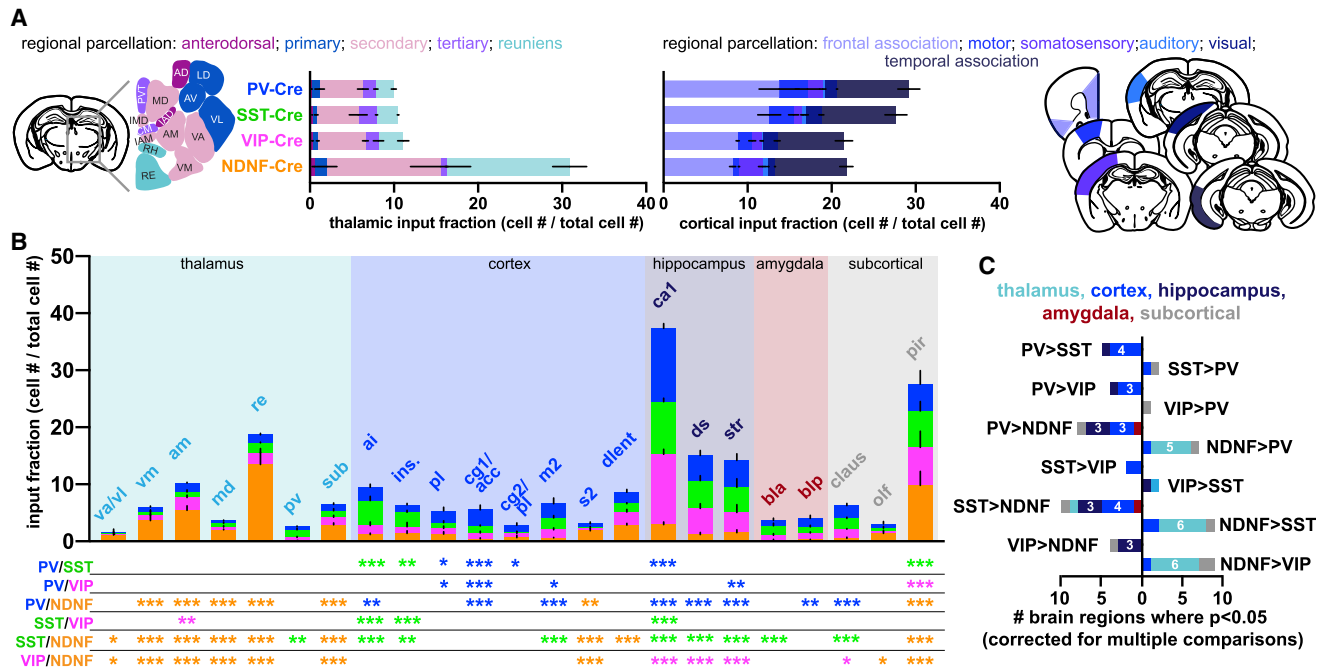
Figure 4. Differences in the input fraction among regions targeting IL interneurons

(A) Proportion of inputs targeting IL interneurons from distinct thalamic groups (left) and cortical information processing modalities (right).

(B) Proportion of inputs from individual brain regions; the asterisks below denote the statistical result (*p < 0.05, **p < 0.005, and ***p < 0.0005 after adjustments for multiple comparisons), and the colors refer to the Cre driver line with the higher input fraction.

(C) The total number of individual brain regions that differ significantly across each pairwise comparison.

For all panels, n = 3 mice for each group except; plots show mean ± SEM. See Figure S5 and Data S1 for additional information and statistical details; see Table S1 for the full names of abbreviated brain regions.

thalamic group and that the proportion of secondary thalamic input differed across projection classes. Specifically, the proportion of secondary thalamic input targeting LEC- or PAG-projecting neurons was ∼2-fold greater than that targeting to BLA-projecting neurons and five-fold greater than those targeting RE-projecting neurons (Figure 5A). Unlike the large differences in input fraction from RE evident in the interneuron dataset, the proportion of input from RE to IL projection classes was similar. Within cortical information processing modalities that project to IL, LEC had larger input fractions from frontal cortical areas relative to both BLA- and RE-projecting neurons; in contrast, BLA- and RE-projecting neurons had significantly greater input fractions from temporal association cortices than LEC-projecting neurons (Figure 5A).

We next examined the input fractions from all brain regions to excitatory projection neurons. Across all presynaptic regions (n = 212), the number of regions that differed in input fraction among the projection classes was similar to the interneuron datasets (BLA versus LEC, 13 regions; BLA versus RE, 8 regions; BLA versus PAG, 10 regions; LEC versus RE, 13 regions, LEC versus PAG, 8 regions; RE versus PAG, 11 regions). The regions in which input fractions differed significantly among the projection classes largely overlapped with those identified in the interneuron datasets across the thalamus (e.g., RE, AM, PV, and Md-Th), cortex (e.g., PL, M2, and DLENT), and hippocampus (e.g., CA1, dorsal subiculum, and subicular transition region)

(Figure 5B). Although the effect sizes were more moderate than those found across the IL interneuron classes, systematic differences in the proportion of inputs from thalamus and hippocampus to projection neurons were evident. For example, BLA and LEC-projecting neurons differed significantly from each other across 13 brain locations, including hippocampus (4 regions) and thalamus (2 regions); LEC-projecting neurons had a greater input fraction from both thalamic regions (AM and Md-Th), while BLA-projecting neurons had a greater input fraction from each of the 4 hippocampal regions (CA1, dorsal subiculum, ventral subiculum, and subicular transition region). Similarly, LEC- and RE-projecting neurons differed from each other in 12 brain regions, including hippocampus (2 regions) and thalamus (4 regions); LEC had greater input from all four thalamic regions (AM, Md-Th, PV, and RE) while RE-projecting neurons had greater input from the CA1 and dorsal subiculum in the hippocampus. In contrast, BLA- and RE-projecting neurons had the fewest differences and did not show a systematic over- or underrepresentation of thalamic or hippocampal inputs (Figures 5B and 5C).

In support of differential connectivity between thalamic and hippocampal regions to IL projection classes, a PCA identified CA1 and AM as the top regions that contribute to the variance among the datasets (28% and 17% of the total variance in principal component 1 [PC1], respectively) (Figure S6). The same correlation-based approach that was used to examine the interneuron classes revealed that LEC and RE-projecting neurons

Table 1. Region names and abbreviations associated with the results shown in Figures 4 and 5

Region name	Abbreviation	Assignment
Ventral anterior /ventrolateral thalamic nucleus	va/vl	thalamus
Ventromedial thalamic nucleus	vm	thalamus
Anteromedial thalamic nucleus	am	thalamus
Mediodorsal thalamic nucleus	md	thalamus
Mediodorsal thalamic nucleus, lateral part	mdl	thalamus
Reuniens thalamic nucleus	re	thalamus
Paraventricular thalamic nucleus	pv	thalamus
Submedius thalamic nucleus	sub	thalamus
Lateral orbital frontal cortex	lo	cortex
Anterior insular cortex	ai	cortex
Insular cortex	ins	cortex
Prelimbic frontal cortex	pl	cortex
Infralimbic frontal cortex	il	cortex
Cingulate cortex, area 1/anterior cingulate cortex	cg1/acc	cortex
Cingulate cortex, area 2/ prelimbic frontal cortex	cg2/pl	cortex
Secondary somatosensory cortex	s2	cortex
Perirhinal cortex	prh	cortex
Dorsolateral entorhinal cortex	dlent	cortex
Field CA1 of the hippocampus	ca1	hippocampus
Dorsal subiculum	ds	hippocampus
Ventral subiculum	versus	hippocampus
Subiculum, transition area	str	hippocampus
Basolateral amygdaloid nucleus, anterior part	bla	amygdala
Basolateral amygdaloid nucleus, posterior part	blp	amygdala
Claustrum	claus	subcortical
Olfactory nerve layer	olf	subcortical
Piriform cortex	pir	subcortical
Dorsal peduncular cortex	dp	subcortical
Lateral septal nucleus	ls	subcortical

had correlations lower than would be expected by chance (Spearman's r = 0.19), while differences between PAG and RE projection neurons matched the lower 2.5% cutoff we used as a bound for statistical significance (Figure S6).

Many of the same regional differences that were evident among the interneuron classes or among the projection neuron classes remained when we analyzed all eight cell classes at once, demonstrating their statistical robustness (Figure S7). Collectively, our results provide strong evidence that both inhibitory and excitatory projection neurons in IL receive input from a widespread and overlapping set of afferent brain regions. However, the proportion of afferent neurons that target these distinct postsynaptic neurons differ, with prominent differences being most evident between hippocampal and thalamic regions. Inter-

estingly, the wiring patterns appear to provide a structural basis for two pathway-specific IL microcircuits (schematized in Figures 6A and 6B).

DISCUSSION

Exactly how networks in the frontal cortex signal task-relevant features to support optimal decision making remains unknown. The frontal cortex integrates information from a widespread number of sensory, motor, emotive, and memory-related brain regions to support the flexible selection of goal-directed behaviors. Previous work has defined the regions that project to or receive projections from rodent frontal cortex (Gabbott et al., 2005; Hoover and Vertes, 2007), though knowledge of the cell-type-specific wiring patterns remains largely unknown. Here, we used monosynaptic, retrograde rabies tracing to map the afferent pathways that converge onto specific frontal cortical inhibitory and excitatory cell classes and uncovered principles that govern how frontal cortical neuron classes are wired into circuits. This resource also reports the analyses of these datasets in an accompanying website (https://raisin.janelia.org), where visitors can make bespoke comparisons between inputs to postsynaptic cell classes and download raw data files.

We focused on the IL cortex and used a two-angle injection approach to limit the spread of starter cells from this area into adjacent cortical regions (though low rates of starter cell transduction was evident in neighboring regions of cortex; see Figure 2). Interestingly, the IL interneurons we examined here all appear to receive the largest fraction of their inputs from long-range afferent circuits. This result differs markedly from recently published work using similar rabies strategies to map connectivity onto PV-Cre, SST-Cre, and VIP-Cre interneurons (Ährlund-Richter et al., 2019; Sun et al., 2019), which reported that the overwhelming fraction of neurons targeting PV-Cre, SST-Cre, and VIP-Cre interneurons were made by local frontal cortical neurons. However, both experiments used a different strain of modified rabies, SAD-B19ΔG, which has been found to label afferent neurons with a lower efficiency than the CVS-N2cΔG strain used here (see Reardon et al., 2016). Thus, our results from both interneurons and projection neurons produce anatomical maps that look substantially different from the existing rabies maps and are more consistent with results provided by traditional retrograde tracers and channelrhodopsin-assisted circuit mapping (CRACM) (Anastasiades et al., 2021; Liu and Carter, 2018).

PV-Cre, SST-Cre, and VIP-Cre interneurons shared highly correlated patterns of afferent inputs across the brain, with the predominant fraction of presynaptic neurons originating in hippocampal region CA1 and the subiculum. Despite such similarity in their broad input patterns, the strength of these synaptic connections (Liu et al., 2020), the unique intrinsic biophysical properties of the postsynaptic neuron classes (e.g., fast-spiking versus adapting), and the specificity of their subsequent postsynaptic targets (e.g., forming synapses onto pyramidal cells or interneurons or somatic or dendritic compartments) (reviewed in Tremblay et al., 2016) permit these different classes to produce different forms of inhibition within the IL microcircuit. NDNF-Cre interneurons, which reside exclusively in layer 1,
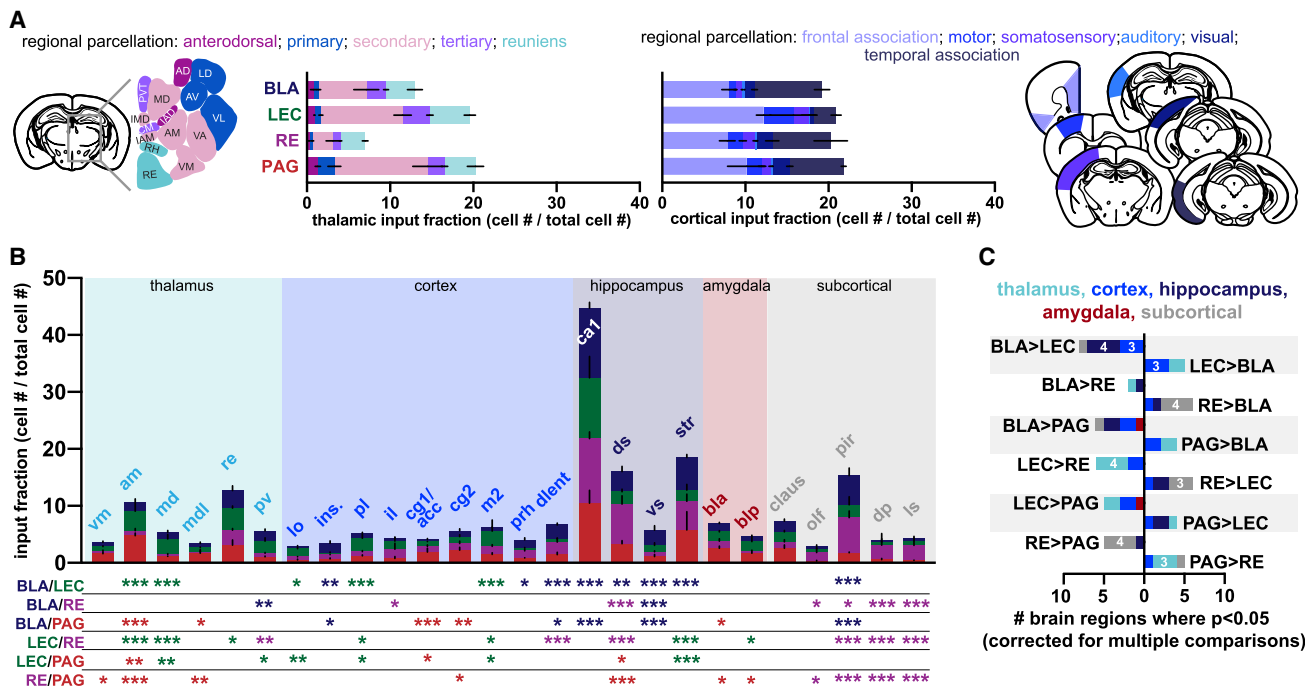
Figure 5. Differences in the input fraction among regions targeting IL projection neurons

(A) Proportion of inputs targeting IL projection neurons from distinct thalamic groups (left) and cortical information processing modalities (right).

(B) Proportion of inputs from individual brain regions; the asterisks below denote the statistical result (*p < 0.05, **p < 0.005, and ***p < 0.0005 after adjustments for multiple comparisons), and the colors refer to the projection with the higher input fraction.

(C) The total number of individual brain regions that differ significantly across each comparison.

For all panels, n = 3 mice for each group, except for n = 5 mice in IL-to-BLA projections; plots show mean ± SEM. See Figure S6 and Data S1 for additional information and statistical details; see Table S1 for the full names of abbreviated brain regions.

had input patterns that were distinctly different from PV-Cre, SST-Cre, and VIP-Cre interneurons. The primary driver of these neurons appeared to be RE rather than CA1, and the correlations between input levels from afferent regions targeting NDNF-Cre and the other interneuron classes were low. Additional brain regions, such as the piriform cortex (which also receives input from RE), showed similarly strong preference for targeting NDNF-Cre interneurons over PV-Cre, SST-Cre, and VIP-Cre interneurons. Collectively, these results provide strong evidence that NDNF interneurons provide a unique form of feedforward inhibition in IL.

We created brain-wide maps of afferent input onto excitatory projection neurons using a RetroAAV approach (Tervo et al., 2016) (similar in spirit to Schwarz et al., 2015). BLA-, RE-, and PAG- projecting frontal cortical neurons have been directly implicated in the top-down control over fear-related behaviors (Bloodgood et al., 2018; Ramanathan et al., 2018; Rozeske et al., 2018), while LEC (but not necessarily IL-to-LEC) may execute similar functions (Xu et al., 2012). Each of the long-range IL projection neurons we examined received their greatest input fraction from area CA1 of the hippocampus, which appears consistent with CRACM of CA1 connections onto IL projection neurons (Liu and Carter, 2018) and the extremely high density of CA1 axons localized to the deeper layers of IL (Liu and Carter, 2018). Despite the large input fraction from CA1, a hippocampus-thalamus input dichotomy remained evident among the pro-

jection classes. Compared to RE-projecting neurons, LEC-projecting IL neurons receive a greater fraction of inputs from multiple thalamic regions and comparably fewer inputs from hippocampus. This pattern (i.e., more from thalamus, fewer from hippocampus and vice versa) also held across more stringent comparisons between projection neuron pairs sharing the same somatic layer and dendritic morphology (e.g., LEC-projecting neurons versus BLA-projecting neurons). Thus, even within neurons that appear to participate in IL's control over fear-related behavior, our results provide strong evidence that different IL output neurons receive distinct patterns of long-range hippocampal and thalamic afferent inputs.

The cellular targeting of midline thalamic regions to layer 1 NDNF-Cre interneurons, and the corresponding spatial targeting of these axons to the most distal portions of the dendritic arbor of pyramidal cells (Anastasiades et al., 2021), creates a local microcircuit in which feedforward inhibition and feedforward excitation interact directly within the distal apical tuft of pyramidal cells. This motif is consistent with CRACM studies in which mouse frontal cortical NDNF interneurons receive strong and robust input from midline thalamus and control distal dendritic Ca^{2+} electrogenesis in frontal cortical pyramidal cells (Anastasiades et al., 2021). The cellular targeting of hippocampal output (e.g., from CA1) to the deeper layers of IL, along with interneurons that target the perisomatic (i.e., from PV-Cre neurons) and apical
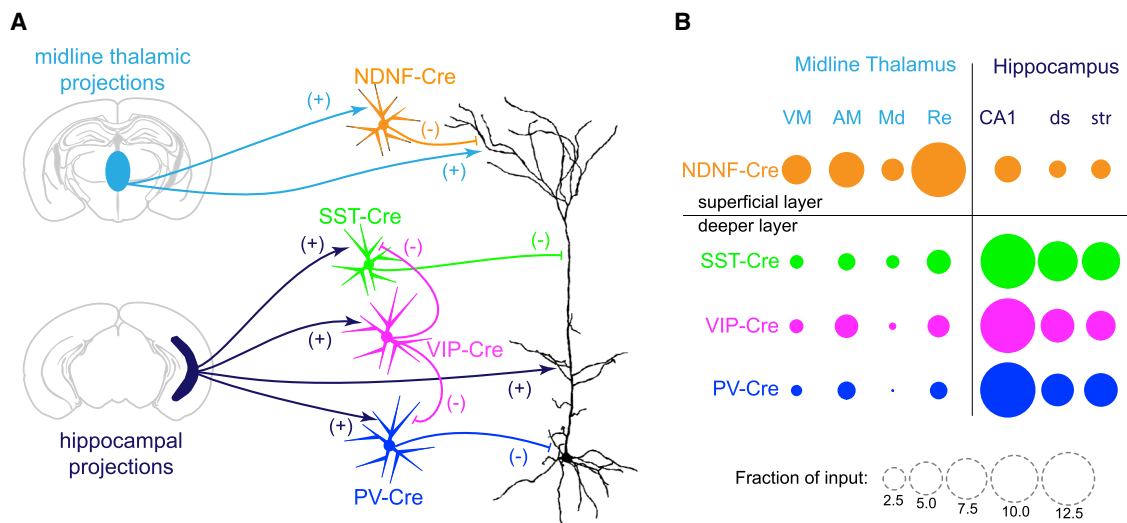
Figure 6. Biased cellular targeting of thalamic and hippocampal afferents suggests the presence of two prominent IL microcircuits
(A) The spatial targeting of thalamic or hippocampal excitatory pathways onto the distal or proximal dendrites of pyramidal cells, coupled with the spatial targeting of inhibitory synapses from these interneuron classes, suggests two prominent feedforward microcircuits controlling the excitability of IL projection neurons.
(B) A graphical depiction of the differential targeting of these afferents to specific IL interneurons.

branches (i.e., from SST-Cre neurons) of the pyramidal cell arbor, creates a second "push-pull" microcircuit in the deeper cortical layers. VIP interneurons, known to preferentially inhibit SST interneurons (Pfeffer et al., 2013), may be driven by CA1 to provide a tunable form of inhibition within this hippocampal-to-IL microcircuit. Determining how these microcircuits interact to shape action potential output, plasticity, and feature selectivity will be a major advance toward understanding the functional role of cell types in frontal cortical-dependent behaviors. A very small number of GFP-labeled neurons in CA1 were located in stratum oriens and may be long-range inhibitory projection neurons; whether and how these inhibitory afferents change the integration of the excitatory input from the neighboring CA1 pyramidal cells can be addressed in future experiments that utilize similar rabies strategies that label specific sets of afferents (Yetman et al., 2019).

The features that govern the functional impact of these specific synapses on dendritic integration or somatic spiking (e.g., the number of synaptic connections, their precise clustered or distributed spatial patterns on the dendrites, and their temporal frequency) cannot be determined by rabies mapping. Compared to CRACM, which typically tests some of these functional features within a single pathway, rabies maps provide a cell-type-specific wiring diagram of all connected presynaptic partners across the entire brain (i.e., a "cell-type-specific projectome"). Despite the lack of functional data presented here, our results suggest a broad and systematic hippocampal-thalamic structural dichotomy that characterizes connectivity onto spatially intermingled neuronal classes in the mouse ventromedial frontal cortex. The patterns of connectivity we find here differ from those in the hippocampus, where inputs to CA1 pyramidal cells from CA3, LEC, or MEC appear to depend on the spatial position of the postsynaptic neuron in area CA1 (i.e., connectivity gradients map well onto spatial gradients) rather than its projection target per se.

Future experiments should use this cell-type-specific anatomical resource to determine how these IL afferent pathways support the emergent computations of IL. Given the large divergence of postsynaptic targets from even a single pathway, these results may spur new approaches to manipulate specific afferent connections rather than whole pathways *in toto*. The emergence of such technology will provide new ways to dissect how the structural organization of synaptic connectivity within cortical circuits contributes to their emergent functions.

STAR★METHODS

Detailed methods are provided in the online version of this paper and include the following:

- KEY RESOURCES TABLE
- RESOURCE AVAILABILITY
  - Lead contact
  - Materials availability
  - Data and code availability
- EXPERIMENTAL MODEL AND SUBJECT DETAILS
  - Ethics statement
  - Animals
- METHOD DETAILS
  - *In situ* hybridization, dual recombinase-dependent reporter labeling, and confocal microscopy
  - Viruses and Intracranial Injections
  - Tissue Processing and Imaging
- QUANTIFICATION AND STATISTICAL ANALYSIS
- ADDITIONAL RESOURCES

REFERENCES

Ährlund-Richter, S., Xuan, Y., van Lunteren, J.A., Kim, H., Ortiz, C., Pollak Dorocic, I., Meletis, K., and Carlén, M. (2019). A whole-brain atlas of monosynaptic input targeting four different cell types in the medial prefrontal cortex of the mouse. Nat. Neurosci. 22, 657–668.

Anastasiades, P.G., Collins, D.P., and Carter, A.G. (2021). Mediodorsal and Ventromedial Thalamus Engage Distinct L1 Circuits in the Prefrontal Cortex. Neuron 109, 314–330.

Barbas, H. (2000). Connections underlying the synthesis of cognition, memory, and emotion in primate prefrontal cortices. Brain Res. Bull. 52, 319–330.

Bloodgood, D.W., Sugam, J.A., Holmes, A., and Kash, T.L. (2018). Fear extinction requires infralimbic cortex projections to the basolateral amygdala. Transl. Psychiatry 8, 60.

Bloss, E.B., Cembrowski, M.S., Karsh, B., Colonell, J., Fetter, R.D., and Spruston, N. (2016). Structured Dendritic Inhibition Supports Branch-Selective Integration in CA1 Pyramidal Cells. Neuron 89, 1016–1030.

Bloss, E.B., Cembrowski, M.S., Karsh, B., Colonell, J., Fetter, R.D., and Spruston, N. (2018). Single excitatory axons form clustered synapses onto CA1 pyramidal cell dendrites. Nat. Neurosci. 21, 353–363.

Cheriyan, J., Kaushik, M.K., Ferreira, A.N., and Sheets, P.L. (2016). Specific Targeting of the Basolateral Amygdala to Projectionally Defined Pyramidal Neurons in Prelimbic and Infralimbic Cortex. eNeuro 3, ENEURO.0002-16.2016.

Collins, D.P., Anastasiades, P.G., Marlin, J.J., and Carter, A.G. (2018). Reciprocal Circuits Linking the Prefrontal Cortex with Dorsal and Ventral Thalamic Nuclei. Neuron 98, 366–379.e4.

Druckmann, S., Feng, L., Lee, B., Yook, C., Zhao, T., Magee, J.C., and Kim, J. (2014). Structured synaptic connectivity between hippocampal regions. Neuron 81, 629–640.

Gabbott, P.L., Warner, T.A., Jays, P.R., Salway, P., and Busby, S.J. (2005). Prefrontal cortex in the rat: projections to subcortical autonomic, motor, and limbic centers. J. Comp. Neurol. 492, 145–177.

Hasegawa, R.P., Blitz, A.M., Geller, N.L., and Goldberg, M.E. (2000). Neurons in monkey prefrontal cortex that track past or predict future performance. Science 290, 1786–1789.

He, M., Liu, Y., Wang, X., Zhang, M.Q., Hannon, G.J., and Huang, Z.J. (2012). Cell-type-based analysis of microRNA profiles in the mouse brain. Neuron 73, 35–48.

Hippenmeyer, S., Kramer, I., and Arber, S. (2004). Control of neuronal phenotype: what targets tell the cell bodies. Trends Neurosci. 27, 482–488.

Hippenmeyer, S., Vrieseling, E., Sigrist, M., Portmann, T., Laengle, C., Ladle, D.R., and Arber, S. (2005). A developmental switch in the response of DRG neurons to ETS transcription factor signaling. PLoS Biol. 3, e159.

Hirokawa, J., Vaughan, A., Masset, P., Ott, T., and Kepecs, A. (2019). Frontal cortex neuron types categorically encode single decision variables. Nature 576, 446–451.

Hoover, W.B., and Vertes, R.P. (2007). Anatomical analysis of afferent projections to the medial prefrontal cortex in the rat. Brain Struct. Funct. 212, 149–179.

Kasthuri, N., Hayworth, K.J., Berger, D.R., Schalek, R.L., Conchello, J.A., Knowles-Barley, S., Lee, D., Vázquez-Reina, A., Kaynig, V., Jones, T.R., et al. (2015). Saturated Reconstruction of a Volume of Neocortex. Cell 162, 648–661.

Kennerley, S.W., and Wallis, J.D. (2009). Evaluating choices by single neurons in the frontal lobe: outcome value encoded across multiple decision variables. Eur. J. Neurosci. 29, 2061–2073.

Lichtman, J.W., and Denk, W. (2011). The big and the small: challenges of imaging the brain's circuits. Science 334, 618–623.

Little, J.P., and Carter, A.G. (2013). Synaptic mechanisms underlying strong reciprocal connectivity between the medial prefrontal cortex and basolateral amygdala. J. Neurosci. 33, 15333–15342.

Liu, X., and Carter, A.G. (2018). Ventral Hippocampal Inputs Preferentially Drive Corticocortical Neurons in the Infralimbic Prefrontal Cortex. J. Neurosci. 38, 7351–7363.

Liu, X., Dimidschstein, J., Fishell, G., and Carter, A.G. (2020). Hippocampal inputs engage CCK+ interneurons to mediate endocannabinoid-modulated feed-forward inhibition in the prefrontal cortex. eLife 9, e55267.

Lovett-Barron, M., Turi, G.F., Kaifosh, P., Lee, P.H., Bolze, F., Sun, X.H., Nicoud, J.F., Zemelman, B.V., Sternson, S.M., and Losonczy, A. (2012). Regulation of neuronal input transformations by tunable dendritic inhibition. Nat Neurosci 15, 423–430.

Luo, L., Callaway, E.M., and Svoboda, K. (2018). Genetic Dissection of Neural Circuits: A Decade of Progress. Neuron 98, 256–281.

Machens, C.K., Romo, R., and Brody, C.D. (2010). Functional, but not anatomical, separation of "what" and "when" in prefrontal cortex. J. Neurosci. 30, 350–360.

Miller, E.K. (2000). The prefrontal cortex and cognitive control. Nat. Rev. Neurosci. 1, 59–65.

Miyamichi, K., Shlomai-Fuchs, Y., Shu, M., Weissbourd, B.C., Luo, L., and Mizrahi, A. (2013). Dissecting local circuits: parvalbumin interneurons underlie broad feedback control of olfactory bulb output. Neuron 80, 1232–1245.

Ongür, D., and Price, J.L. (2000). The organization of networks within the orbital and medial prefrontal cortex of rats, monkeys and humans. Cereb. Cortex 10, 206–219.

Paxinos, G., and Franklin, K.B.J. (2004). The mouse brain in stereotaxic coordinates, Compact, Second Edition (Elsevier Academic Press).

Pfeffer, C.K., Xue, M., He, M., Huang, Z.J., and Scanziani, M. (2013). Inhibition of inhibition in visual cortex: the logic of connections between molecularly distinct interneurons. Nat. Neurosci. 16, 1068–1076.

Phillips, J.W., Schulmann, A., Hara, E., Winnubst, J., Liu, C., Valakh, V., Wang, L., Shields, B.C., Korff, W., Chandrashekar, J., et al. (2019). A repeated molecular architecture across thalamic pathways. Nat. Neurosci. 22, 1925–1935.

Ramanathan, K.R., Jin, J., Giustino, T.F., Payne, M.R., and Maren, S. (2018). Prefrontal projections to the thalamic nucleus reuniens mediate fear extinction. Nat. Commun. 9, 4527.

Reardon, T.R., Murray, A.J., Turi, G.F., Wirblich, C., Croce, K.R., Schnell, M.J., Jessell, T.M., and Losonczy, A. (2016). Rabies Virus CVS-N2c(ΔG) Strain

Enhances Retrograde Synaptic Transfer and Neuronal Viability. Neuron *89*, 711–724.

Rigotti, M., Barak, O., Warden, M.R., Wang, X.J., Daw, N.D., Miller, E.K., and Fusi, S. (2013). The importance of mixed selectivity in complex cognitive tasks. Nature *497*, 585–590.

Royer, S., Zemelman, B.V., Losonczy, A., Kim, J., Chance, F., Magee, J.C., and Buzsáki, G. (2012). Control of timing, rate and bursts of hippocampal place cells by dendritic and somatic inhibition. Nat. Neurosci. *15*, 769–775.

Rozeske, R.R., Jercog, D., Karalis, N., Chaudun, F., Khoder, S., Girard, D., Winke, N., and Herry, C. (2018). Prefrontal-Periaqueductal Gray-Projecting Neurons Mediate Context Fear Discrimination. Neuron *97*, 898–910.e6.

Schneider, C.A., Rasband, W.S., and Eliceiri, K.W. (2012). NIH Image to ImageJ: 25 years of image analysis. Nature Methods *9*, 671–675.

Schwarz, L.A., Miyamichi, K., Gao, X.J., Beier, K.T., Weissbourd, B., DeLoach, K.E., Ren, J., Ibanes, S., Malenka, R.C., Kremer, E.J., and Luo, L. (2015). Viral-genetic tracing of the input-output organization of a central noradrenaline circuit. Nature *524*, 88–92.

Sun, Q., Li, X., Ren, M., Zhao, M., Zhong, Q., Ren, Y., Luo, P., Ni, H., Zhang, X., Zhang, C., et al. (2019). A whole-brain map of long-range inputs to GABAergic interneurons in the mouse medial prefrontal cortex. Nat. Neurosci. *22*, 1357–1370.

Taniguchi, H., He, M., Wu, P., Kim, S., Paik, R., Sugino, K., Kvitsiani, D., Fu, Y., Lu, J., Lin, Y., et al. (2011). A resource of Cre driver lines for genetic targeting of GABAergic neurons in cerebral cortex. Neuron *71*, 995–1013.

Tasic, B., Menon, V., Nguyen, T.N., Kim, T.K., Jarsky, T., Yao, Z., Levi, B., Gray, L.T., Sorensen, S.A., Dolbeare, T., et al. (2016). Adult mouse cortical cell taxonomy revealed by single cell transcriptomics. Nat. Neurosci. *19*, 335–346.

Tervo, D.G., Hwang, B.Y., Viswanathan, S., Gaj, T., Lavzin, M., Ritola, K.D., Lindo, S., Michael, S., Kuleshova, E., Ojala, D., et al. (2016). A Designer AAV Variant Permits Efficient Retrograde Access to Projection Neurons. Neuron *92*, 372–382.

Tremblay, R., Lee, S., and Rudy, B. (2016). GABAergic Interneurons in the Neocortex: From Cellular Properties to Circuits. Neuron *91*, 260–292.

Ugolini, G. (2011). Rabies virus as a transneuronal tracer of neuronal connections. Adv. Virus Res. *79*, 165–202.

Wall, N.R., Wickersham, I.R., Cetin, A., De La Parra, M., and Callaway, E.M. (2010). Monosynaptic circuit tracing in vivo through Cre-dependent targeting and complementation of modified rabies virus. Proc. Natl. Acad. Sci. USA *107*, 21848–21853.

Weissbourd, B., Ren, J., DeLoach, K.E., Guenthner, C.J., Miyamichi, K., and Luo, L. (2014). Presynaptic partners of dorsal raphe serotonergic and GABAergic neurons. Neuron *83*, 645–662.

Wickersham, I.R., Lyon, D.C., Barnard, R.J., Mori, T., Finke, S., Conzelmann, K.K., Young, J.A., and Callaway, E.M. (2007). Monosynaptic restriction of transsynaptic tracing from single, genetically targeted neurons. Neuron *53*, 639–647.

Xu, W., Morishita, W., Buckmaster, P.S., Pang, Z.P., Malenka, R.C., and Südhof, T.C. (2012). Distinct neuronal coding schemes in memory revealed by selective erasure of fast synchronous synaptic transmission. Neuron *73*, 990–1001.

Yetman, M.J., Washburn, E., Hyun, J.H., Osakada, F., Hayano, Y., Zeng, H., Callaway, E.M., Kwon, H.B., and Taniguchi, H. (2019). Intersectional monosynaptic tracing for dissecting subtype-specific organization of GABAergic interneuron inputs. Nat. Neurosci. *22*, 492–502.

Cell Reports
Resource

STAR★METHODS

KEY RESOURCES TABLE

REAGENT or RESOURCE	SOURCE	IDENTIFIER
Bacterial and virus strains		
AAVRetro-Cre	Janelia Research Campus; Tervo et al., 2016	N/A
AAVRetro-FLPo	This paper; Janelia Research Campus	N/A
AAVRetro-H2B_tdTomato	This paper; Janelia Research Campus	N/A
AAV2/1-CamK2-Cre	This paper; Janelia Research Campus	N/A
AAV2/1-CAG-flex-EGFP	This paper; Janelia Research Campus	N/A
AAV2/1-CAG-flex-*rev*-tdTomato	This paper; Janelia Research Campus	N/A
AAV2/1-CAG-frt-*rev*-EGFP	This paper; Janelia Research Campus	N/A
AAV2/1-CGA-flex-*rev*-TVA-2a-mKate2	This paper; Janelia Research Campus	N/A
AAV2/1-CGA-flex-*rev*-ΔG-2a-mKate2	This paper; Janelia Research Campus	N/A
CVS-N2cΔG EGFP(EnvA)	Reardon et al., 2016; Janelia Research Campus	N/A
Deposited data		
Raw and analyzed data	This paper	Figshare: https://dx.doi.org/10.6084/m9.figshare.13302731
Experimental models: Organisms/strains		
C57BL6/J	The Jackson Laboratory; stock# 005304	RRID:IMSR_JAX:000664
PV-Cre mice: C57BL6/J:*Pvalb*$^{tm1(cre)Arbr}$	The Jackson Laboratory; JAX stock# 008069	RRID:IMSR_JAX:008069
SST-Cre mice: C57BL6/J:*Sst-ires-Cre*	(Lovett-Barron et al., 2012)	Dr. Boris Zemelman /Janelia Research Campus
VIP-Cre mice: C57BL6/J:*Vip*$^{tm1(cre)Zjh}$/*AreckJ*	The Jackson Laboratory; JAX stock# 031628	RRID:IMSR_JAX:031628
NDNF-Cre mice: C57BL6/J:Ndnf$^{tm1.1(folA/cre)Hze}$	The Jackson Laboratory; JAX stock# 028356	RRID:IMSR_JAX:028536
Software and Algorithms		
ImageJ	(Schneider et al., 2012)	https://imagej.nih.gov/ij/
Other		
Resource website for the publication	This paper	Figshare: https://dx.doi.org/10.6084/m9.figshare.13302731
Resource website for the publication	This paper	RAISIN: https://raisin.janelia.org/

RESOURCE AVAILABILITY

Lead contact
Further information and requests for resources and reagents should be directed to and will be fulfilled by the Lead Contact, Dr. Erik Bloss (erik.bloss@jax.org).

Materials availability
This study did not generate new unique reagents.

Data and code availability
The raw images and data for the figures have been deposited at figshare (https://figshare.com/articles/dataset/Datasets_and_images_
for_the_figures_in_Hippocampal_and_thalamic_afferents_form_distinct_synaptic_microcircuits_in_the_mouse_frontal_cortex_by_

Graham_et_al_/13302731/1) and at (https://raisin.janelia.org) and are publicly available as of the date of publication. DOIs are listed in the key resources table. Any additional information required to reanalyze the data reported in this paper is available from the lead contact upon request. This paper does not report original code.

EXPERIMENTAL MODEL AND SUBJECT DETAILS

Ethics statement

All experiments were conducted in accordance with NIH guidelines and with approval of the Janelia Institutional Animal Care and Use Committee (Protocol 14-118). Authors performed their work following guidelines established by the ''The Eighth Edition of the Guide for the Care and Use of Laboratory Animals'' and euthanasia using methods approved by the American Veterinary Medical Association.''

Animals

Adult C57BL/6J male mice (between 10-16 weeks of age) were used for the tracer and AAV experiments in Figure S1, for the overlap of projection neurons in Figures 2 and S2, for the CVS-N2cΔG GFP(EnvA) control experiments designed to test the leak of AAV and RabV reagents in Figure S3, and for all experiments that used AAVRetro-Cre to map afferent neurons targeting IL projection neurons. Homozygous Rosa26-LSL_GFP-H2B (He et al., 2012) mice were used for the AAVRetro-Cre experiments shown in Figure S1. Heterozygous transgenic mice with an ires-Cre coding sequence inserted into the promoter region of the *pv* (Hippenmeyer et al., 2005), *sst* (Royer et al., 2012), *vip* (Taniguchi et al., 2011), or *ndnf* (Tasic et al., 2016) loci were used to gain access to distinct sets of interneurons. In all experiments, mice were single housed after surgery in a 12-h/12 h light/dark cycle with food and water available *ad libitum*. Mice were assigned to experimental conditions based upon their availability.

METHOD DETAILS

In situ hybridization, dual recombinase-dependent reporter labeling, and confocal microscopy

To examine the specificity, efficiency, and cellular overlap of each transgenic Cre driver line in IL (shown in Figure 1), 20 μm-thick cryostat sections of perfusion fixed brains were used for RNAscope fluorescent triple-label *in situ* hybridization according to the manufacturer's instructions and with commercially-available reagents (Advanced Cell Diagnostics; similar to Bloss et al., 2016). Tiled z stacks of IL were acquired using a Zeiss 710 confocal microscope equipped with a 20x objective and ZEN software, and images were quantified using the cell counter plugin for Fiji. To measure the cellular overlap of IL neurons projecting to different target sites, 150 μm-thick sections containing IL tdTomato or GFP-expressing projection neurons were imaged using a Zeiss 710 confocal microscope equipped with a 40x objective and ZEN software. The fraction of single and dual labeled neurons was counted using the cell counter plugin for Fiji. In both experiments, the distance of the labeled cell from the pial surface was recorded to obtain the data in Figure S2. For the dendritic morphological reconstructions, interneurons and projection neurons labeled by Cre- or FLPo-dependent reporter viruses were acquired with a Zeiss 710 confocal microscope equipped with a 40x objective and ZEN software, TIFF stacks were imported into NeuronStudio, and dendritic morphologies were manually reconstructed and analyzed using a Sholl analysis.

Viruses and Intracranial Injections

Adeno-associated viruses were prepared at Janelia Research Campus, and titers were as follows: AAVRetro-Cre, 1e13 GC/mL; AAVRetro-FLPo, 1e13 GC/mL; AAVRetro-tdTomato-H2B, 1e13 GC/mL; AAV2/1-CamKII-Cre, 4e13 GC/mL; AAV2/1-CAG-flex-rev-GFP, 1e13 GC/mL; AAV2/1-CAG-flex-rev-mKate2-T2A-N2c-G, 2e13 GC/mL; AAV2/1-CAG-flex-rev-mKate2-T2A-TVA, 1e13 GC/mL; and CVS-N2cΔG GFP(EnvA), 1e9 IU/mL. Injection volumes were chosen to minimize spread into the adjacent motor or prelimbic cortices and were the following: WGA-555 (Sigma) and CTB-555, both 36 nL per site; AAVRetroCre, 27 nL per site. For IL injection of AAV2/1-CAG-flex-rev-mKate2-T2A-N2c-G and AAV2/1-CAG-flex-rev-mKate2-T2A-TVA, the two viral constructs were mixed at a 2:1 ratio. The methodology and details for intracranial injections of tracers and viruses was identical to that described in (Bloss et al., 2016). For experiments in which IL was targeted by a pair of injections (e.g., in all rabies experiments where an initial injection of AAVs was followed by injection of CVS-N2cΔG), the first IL injections of AAVs were made with the mouse at a 0° tilt, and the subsequent RabV was injected with the mouse at a 15° tilt to avoid inadvertent transduction of neurons along the first pipette tract. At all sites, high-titer viral suspension (18-54 nl) was injected over 5 minutes at the following coordinates (in mm relative to bregma, lateral relative to midline, and ventral relative to pial surface):

IL: (+1.75, 0.3, 2.25); IL at 15° tilt: (+1.75, 0.95, 2.6); BLA: (−1.6, 3.3, 4.1); PAG, (−4.75, 0.5, 2 and 1.5); LEC: (−4.2, 4.5, 2.5); RE at 15° tilt (−1.2 and −1.5,1.2, 4.2).

Also see Data S1. Full names and abbreviations for brain regions. Related to Figures 2, 3, 4, and 5.

Tissue Processing and Imaging

Mice were sacrificed by transcardial perfusion at the following time points after intracranial injection: WGA, 24 hours; CTB, 1 week; AAVRetro-Cre (for Figure S1), 2 weeks; AAVRetro-tdTomato-H2B, 2 weeks; AAV-rev-flex-GFP, 2 weeks; RabV, one week. At sacrifice, mice were transcardially perfused with 5 mLs of ice-cold 1% depolymerized paraformaldehyde in 0.1M PB (pH 7.3), followed by 50 mls of ice-cold 4% paraformaldehyde in 0.1M PB (pH 7.3) at 10 mLs/min. Brains were postfixed in the same fixative overnight at 4°C, then transferred to 0.1M PB, cut into sequential 50 μm-thick vibratome sections, mounted onto microscope slides and coverslipped with Vectashield HardSet containing DAPI.

Images of coronal sections (from 2.68 mm anterior to Bregma to −4.6mm posterior to Bregma) were collected on a TissueFaxs 200 confocal microscope (TissueGnostics, Vienna, Austria) comprising an X-Light V2 spinning disk confocal imaging system (CrestOptics, Rome, Italy) built on an Axio Imager.Z2 microscope (Carl Zeiss Microscopy, White Plains, NY) and equipped with a 10x, 0.3 NA objective (Zeiss) and an Zyla 5.5 sCMOS camera (Andor, Belfast, UK). DAPI, GFP, and mKate2 were excited with a Spectra X light engine (Lumencor, Beaverton, OR).

Z stacks (3 μm step) were collected to collect data from the entire slice, but only maximum intensity projections were analyzed. Exposure times were kept constant throughout the study for all three channels, though the dynamic range of the exported 16-bit images was adjusted to correct for the mild differences in signal intensity between samples. Assembled slice montages were exported as 16-bit images then transformed to 8-bit images during alignment to (Paxinos and Franklin, 2004). Briefly, individual coronal slices were registered via affine transformations in trakEM2 (Fiji) using the tissue edges and various internal reference marks (e.g., ventricles or white-matter tracts). GFP+ and mKate2+ neurons were counted and assigned to specific brain regions using intensity-based thresholds. False negative and Positive rates of this counting procedure are shown in Figure S3.

Also see Data S1. Supplemental Statistics. Related to Figures 2, 3, 4, and 5

QUANTIFICATION AND STATISTICAL ANALYSIS

All statistical comparisons and results are reported in Data S2, including all p values (considered statistically significant at $p < 0.05$ after any corrections for multiple comparisons). Briefly, all two-way ANOVAs (e.g., in Figures 3D, 4B–4D, 5A, 5B, 6A, 6B, S2B, S2D, and S3C) used Tukey's posthoc tests with adjustments for multiple comparisons, and all correlations (e.g., Figures 3E, S3B, S5C, and S6C) used two-tailed nonparametric Spearman's correlations; these datasets were tested for normality and analyzed using GraphPad Prism 8. Principal component analyses were run on R using the prcomp package. Figures in the paper depict mean ± SEM.

Also see Data S2. Supplemental Raw Data. Related to Figures 3, 4, and 5.

ADDITIONAL RESOURCES

We have created a public resource to accompany this publication, rabies-assisted interrogation of synaptic infralimbic networks (or RAISIN; https://raisin.janelia.org), that provides analysis and visualization of the datasets reported in this paper.